Monthly Notices
of the
ROYAL ASTRONOMICAL SOCIETY

MNRAS **494,** 349–362 (2020)
Advance Access publication 2020 March 20

doi:10.1093/mnras/staa745

Setting the scene for BUFFALO: a study of the matter distribution in the HFF galaxy cluster MACS J0416.1−2403 and its parallel field

E. J. Gonzalez,[1,2,3]★ M. Chalela,[1,2] M. Jauzac,[4,5,6] D. Eckert,[7] M. Schaller,[8] D. Harvey,[9] A. Niemiec,[10] A. M. Koekemoer,[11] D. Barnes,[12] D. Clowe,[13] T. Connor,[14] J. M. Diego,[15] J. D. Remolina Gonzalez[10] and C. L. Steinhardt[16,17,18]

[1]*Instituto de Astronomía Teórica y Experimental, (IATE-CONICET), Laprida 854, X5000BGR Córdoba, Argentina*
[2]*Observatorio Astronómico de Córdoba, Universidad Nacional de Córdoba, Laprida 854, X5000BGR Córdoba, Argentina*
[3]*Centro Brasileiro de Pesquisas Físicas, Rio de Janeiro, RJ 22290-180, Brazil*
[4]*Centre for Extragalactic Astronomy, Durham University, South Road, Durham DH1 3LE, UK*
[5]*Institute for Computational Cosmology, Durham University, South Road, Durham DH1 3LE, UK*
[6]*Astrophysics and Cosmology Research Unit, School of Mathematical Sciences, University of KwaZulu-Natal, Durban 4041, South Africa*
[7]*Astronomy Department, University of Geneva, 16 ch. d'Ecogia, CH-1290 Versoix, Switzerland*
[8]*Leiden Observatory, Leiden University, PO Box 9513, 2300 RA Leiden, the Netherlands*
[9]*Instituut-Lorentz for Theoretical Physics, Universiteit Leiden, Niels Bohrweg 2, Leiden, P.O. Box 9506, the Netherlands*
[10]*Department of Astronomy, University of Michigan, 1085 South University Ave, Ann Arbor, MI 48109, USA*
[11]*Space Telescope Science Institute, 3700 San Martin Dr., Baltimore, MD 21218, USA*
[12]*Department of Physics, MIT Kavli Institute for Astrophysics and Space Research, Cambridge, MA 02139, USA*
[13]*Department of Physics and Astronomy, Ohio University, Clippinger Labs 251B, Athens, OH 45701, USA*
[14]*The Observatories of the Carnegie Institution for Science, 813 Santa Barbara St, Pasadena, CA 91101, USA*
[15]*Instituto de Física de Cantabria (CSIC-UC), Edificio Juan Jordá, Avda Los Castros s/n. 39005 Santander, Spain*
[16]*Cosmic Dawn Center (DAWN), Lyngbyvej 2, DK-2100 Copenhagen, Denmark*
[17]*Niels Bohr Institute, University of Copenhagen, Lyngbyvej 2, DK-2100 Copenhagen, Denmark*
[18]*DARK, Niels Bohr Institute, University of Copenhagen, Lyngbyvej 2, DK-2100 Copenhagen, Denmark*

Accepted 2020 March 11. Received 2020 February 27; in original form 2019 December 9

ABSTRACT

In the context of the Beyond Ultradeep Frontier Fields And Legacy Observations (BUFFALO) survey, we present a new analysis of the merging galaxy cluster MACS J0416.1−2403 ($z = 0.397$) and its parallel field using Hubble Frontier Fields (HFF) data. We measure the surface mass density from a weak-lensing analysis and characterize the overall matter distribution in both the cluster and parallel fields. The surface mass distribution derived for the parallel field shows clumpy overdensities connected by filament-like structures elongated in the direction of the cluster core. We also characterize the X-ray emission in the parallel field and compare it with the lensing mass distribution. We identify five mass peaks at the $>5\sigma$ level over the two fields, four of them being in the cluster one. Three of them are located close to galaxy overdensities and one is also close to an excess in the X-ray emission. Nevertheless, two of them have neither optical nor X-ray counterpart and are located close to the edges of the field of view, thus further studies are needed to confirm them as substructures. Finally, we compare our results with the predicted subhalo distribution of one of the Hydrangea/C-EAGLE simulated cluster. Significant differences are obtained suggesting the simulated cluster is at a more advanced evolutionary stage than MACS J0416.1−2403. Our results anticipate the upcoming BUFFALO observations that will link the two HFF fields, extending further the *HST* coverage.

Key words: gravitational lensing: weak – galaxies: clusters: individual: MACS J0416.1−2403 – cosmology: observations – dark matter – X-rays: galaxies: clusters.

★ E-mail: ejgonzalez@unc.edu.ar

1 INTRODUCTION

Massive clusters of galaxies act as natural telescopes by deflecting and magnifying the light emitted by galaxies behind them due to the gravitational lensing (e.g. see reviews Wambsganss 2006; Kneib 2010; Kneib & Natarajan 2011; Bartelmann & Maturi 2017). Taking advantage of this, the *Hubble Space Telescope* (*HST*) observed six of the most massive known clusters of galaxies in the context of the Hubble Frontier Fields (HFF; Lotz et al. 2017) programme. The HFF combine the capabilities of *HST* with the magnification power of massive galaxy clusters. The programme observed six massive strong-lensing clusters and six parallel 'blank' fields (4 arcmin away from the central field), in order to detect the faintest galaxies and to obtain hints regarding galaxy evolution at early times.

The main scientific goals of the HFF, are to explore the high-redshift Universe characterizing galaxies at $z > 5$, and to set the scene for the coming *James Webb Space Telescope* (*JWST*). Following a similar philosophy, the Beyond Ultra-deep Frontier Fields And Legacy Observations (BUFFALO; Steinhardt et al. 2018) survey expands the spatial coverage of the HFF clusters with *HST* out to 3/4 $\times$ $R_{\rm vir}$ (where $R_{\rm vir}$ is the virial radius), and covers the unobserved regions between the HFF cluster and the parallel fields. BUFFALO will place constraints on the formation of massive and luminous high-redshift galaxies as well as study how dark matter, gas, and dynamics influence clusters and their surroundings. In particular, the analysis of substructures in massive clusters can be used as a test for the standard model of cosmology, lambda cold dark matter (ΛCDM). Detected substructures in cluster surroundings can be compared with the subhalo mass function predicted by simulations (e.g. Springel et al. 2001; Natarajan & Springel 2004; Natarajan, De Lucia & Springel 2007; Grillo et al. 2015; Steinhardt et al. 2016; Schwinn et al. 2017; Jauzac et al. 2018). Moreover, comparisons between the observed and predicted radial distribution of substructures for the subhaloes in simulations provide an additional test to the current cosmological paradigm.

It is important to have detailed measurements of the mass distributions of the HFF clusters in order to use them as natural telescopes. In this sense, gravitational lensing has proved to be a powerful tool to constrain the line of sight projected surface mass distribution of galaxy systems. Strong lensing in particular, in which the images of source galaxies are strongly distorted and observed as arcs and multiple images, provides information on the inner regions of galaxy systems (e.g. Diego et al. 2007; Zitrin et al. 2009; Vegetti et al. 2010; Lam et al. 2014; Sharon & Johnson 2015; Jauzac et al. 2015b; Reed et al. 2018; Williams, Sebesta & Liesenborgs 2018; Acebron et al. 2019; Mahler et al. 2019; Sharon et al. 2019). At the same time, weak gravitational lensing is a powerful statistical tool that provides information regarding the projected mass distribution of galaxy systems at larger distances from their centres and allows to obtain the total masses of the dark matter haloes (e.g. Wegner & Heymans 2011; Dietrich et al. 2012; Jauzac et al. 2012; Jullo et al. 2014; Umetsu et al. 2014; Gonzalez et al. 2018). The combination of both techniques allows us to obtain a well-constrained mass distribution at small and larger distances from the cluster centres, which subsequently helps us to recover the distribution of lower mass dark matter substructures (Diego et al. 2007; Sereno & Umetsu 2011; Jauzac et al. 2015a, 2016, 2018).

In view of the forthcoming BUFFALO observations, we present an analysis of the massive HFF cluster, MACS J0416.1−2403 ($z = 0.397$, hereafter MACS J0416). This cluster was discovered by the Massive Cluster Survey (MACS; Ebeling, Edge & Henry 2001), and was classified as a merging system according to its X-ray emission (Mann & Ebeling 2012) that shows a double-peaked profile and a very elongated gas distribution. This scenario is confirmed by the strong lensing analysis presented by Jauzac et al. (2014). Based on a set of 57 multiply imaged systems, the best-fitting model includes two cluster-scale dark matter haloes, with a velocity dispersion of 778 and 955 km s^{-1}, respectively, and 98 galaxy-scale haloes. This study was extended by including weak lensing to model the surroundings of the cluster core (Jauzac et al. 2015a; hereafter J15) from which a third massive structure was detected in the south−west direction from the cluster centre. Despite the complex structure of MACS J0416 and its merging characteristics, a good correlation between mass and light is observed in this system (Sebesta et al. 2016). This cluster was also used to identify halo substructure from a lensing analysis using masses lower than 10^{13} M$_{\odot}$. Derived results were compared with the subhalo mass functions predicted by numerical simulations. Grillo et al. (2015) found that simulated galaxy clusters with a mass comparable to MACS J0416, contain considerably less mass in subhaloes in their cores than the one inferred from a strong-lensing analysis. A posterior analysis found a good correlation between the predictions from simulations and the lensing inferred substructures, but reported discrepancies regarding the radial distribution of the detected subhaloes (Natarajan et al. 2017).

In this work, we present a new optical analysis of the MACS J0416 cluster and parallel fields, complemented by an X-ray study of the parallel field that will be completed by the BUFFALO survey. The MACS J0416 parallel field was selected to lie west of the cluster in order to avoid the bright eastern stars. This orientation is perpendicular to the elongation of the cluster on the sky, so no significant mass distribution associated with the cluster is expected in this field. In this work, we pursue a new weak-lensing study of the mentioned fields, which we combine with previous strong-lensing results in order to derive the projected surface mass density of the cluster and its parallel. This approach allows to map the density distribution in the outskirts of the cluster and to detect the presence of subhaloes, since the strong lensing information sets the location and shape of the cluster core while the weak-lensing traces the mass distribution at larger scales. The resulting surface distribution is then put in perspective of the optical and X-ray emission distributions. From the derived lensing projected mass distribution, we also identify substructures present in these fields and compare our results with predictions from numerical simulations.

The paper is organized as follows. In Sections 2 and 3, we describe the observational and simulated data used to perform the analysis, respectively. In Section 4, we describe the shape measurements and define the criterion for the galaxy classification for the weak-lensing analysis. In Section 5, we characterize the method used to obtain the projected mass distribution from the shape measurements. We present our results in Section 6. Finally, we discuss our results in Section 7. Throughout the analysis, we adopt a standard cosmological model: $H_0 = 70$ km s^{-1} Mpc, $\Omega_{\rm m} = 0.3$, and $\Omega_{\Lambda} = 0.7$. All magnitudes are quoted in the AB system.

2 OBSERVATIONS

2.1 *Hubble Space Telescope*

MACS J0416 was first observed using *HST* in 2007 under the SNAPshot programme GO-11103 (PI: Ebeling) using the Wide Field and Planetary Camera 2 (WFPC2). These observations pointed at MACS J0416 as a powerful lens, which led to the inclusion of

Table 1. Summary of the *HST* observations used in this work.

Field	RA (J2000)	Dec. (J2000)	Number of combined exposures	Date range of observations	Instrument/filter	Exposure time (in seconds)
Cluster	04:16:08.9	−24:04:28.7	40	2014-02-21/22	ACS/*F*435*W*	54 512
			24		ACS/*F*606*W*	33 494
			96		ACS/*F*814*W*	129 941
Parallel	04:16:33.1	−24:06:50.6	36	2014-09-05	ACS/*F*435*W*	45 747
			20		ACS/*F*606*W*	25 035
			83		ACS/*F*814*W*	105 498

this cluster in the CLASH programme (PI: Postman; Postman et al. 2012). The cluster was observed again in 2012 for a total of 20 orbits across 16 pass-bands, from the UV to the near-IR. The obtained data were used for the pre-HFF analysis of the cluster.[1] More information regarding these images can be found in J15.

For the lensing analysis, we use the same data set as the one described in J15, based on the observations taken with the Advanced Camera for Surveys (ACS). We also include in our analysis the parallel 'blank' field images in the same filters as for the cluster field (*F*435*W*, *F*606*W*, and *F*814*W*). All of these HFF observations were performed under the observing programme GO-13496 (PI: Lotz, Lotz et al. 2017).

Reduced images were obtained after applying basic data-reduction procedures, using HSTCAL and the most recent calibration files. Individual frames were co-added for each filter, using ASTRODRIZZLE after registration to a common ACS reference image using TWEAKREG. ASTRODRIZZLE generates the drizzled images, correcting for the geometric distortion that is produced since ACS is located off-axis in the *HST* focal plane and the ACS focal plane is not normal to incident light rays. This is done simultaneously removing cosmic rays and bad pixels, as well as combining multiple exposures into a single output image. More details on these types of procedures are presented in Koekemoer et al. (2011). Final stacked images have a pixel size of 0.03 arcsec. A summary of the observations and some of their characteristics is provided in Table 1.

2.2 Spectroscopic and photometric redshifts

We make use of the HFF-DeepSpace photometric catalogues of the twelve HFF presented in Shipley et al. (2018). These catalogues were constructed using all data publicly available from space and ground-based observations. These include *HST*/WFC3, *HST*/ACS, *Spitzer Space Observatory*/IRAC, the *Very Large Telescope*/HAWK-I, and *Keck-I*/MOSFIRE, providing a total of 22 filters for photometry, and thus photometric redshifts of excellent quality. Photometric redshifts were computed with the EAZY software (Brammer, van Dokkum & Coppi 2008). To asses their quality, all spectroscopic redshifts available in the literature were used (only from sources that targeted the *HFF* clusters), achieving an average scatter of $\sigma \sim 0.034$ between photometric and spectroscopic redshifts. These spectroscopic redshifts are also included in the HFF-DeepSpace catalogues.

For the cluster and parallel fields of MACS J0416 there are 378 and 79 spectroscopic redshifts, respectively, listed from different sources: Jauzac et al. (2014), Ebeling, Ma & Barrett (2014), Grillo et al. (2015), GLASS (Treu et al. 2015), Balestra et al. (2016), Caminha et al. (2017), and Brammer et al. (in preparation). All of these redshifts, as well as the photometry provided in the HFF-DeepSpace catalogues, in particular the *F*435*W*, *F*606*W*, and *F*814*W* pass-bands corrected for galactic extinction, are used in our analysis for the selection of background galaxies, and the identification of cluster members. Following the prescriptions of Shipley et al. (2018), we restrict the galaxies used in this work to those with flag use_phot = 1 and with a strict cut in the photometry signal-to-noise ratio of >10 (further details on these parameters can be found in section 3.10 of Shipley et al. 2018).

2.3 *Chandra X-ray observatory*

We compare the derived surface mass density distribution derived for the parallel field with the X-ray emission using the X-ray data provided by *Chandra*. MACS J0416 was observed by *Chandra*/ACIS-I on six occasions between 2009 June and 2014 December (observation ID 10446, 16236, 16237, 16304, 16523, and 17313) for a total of 324 ks. The full data set was analysed in detail in Ogrean et al. (2015). We reprocessed the six individual observations using the CIAO v4.8 package and CALDB v.4.7.2 with the `chandra_repro` tool. We inspected the light curves of each individual observation to remove periods of flaring background and create clean event files. The individual event files were then merged using the `merge_obs` utility. We extracted images and exposure maps in the [0.5–2] keV energy band from the merged event files using `fluximage` tool. Finally, we used a collection of blank-sky images to estimate a local background map by reprojecting the events along the telescope's attitude (Hickox & Markevitch 2006).

3 SIMULATIONS

From the lensing surface mass density distribution, we detect subhaloes present in the cluster and parallel fields. The derived substructures and their distribution are compared with simulations. We perform a similar analysis as the one presented in Jauzac et al. (2018) by comparing our lensing detected subhaloes with the ones detected in a simulated cluster similar to MACS J0416. In order to do that, we use the Hydrangea/C-EAGLE simulation (Bahé et al. 2017; Barnes et al. 2017), a set of cosmological hydrodynamical zoom-in simulations of the formation of 30 galaxy clusters in the mass range $10^{14} < M_{200}/\mathrm{M}_{\odot} < 10^{15}$ (where M_{200} is the mass within a radius that encloses a mean density equal to 200 times the critical density of the Universe at the cluster redshift). The clusters were selected from a parent, dark matter only simulation of 3.2 Gpc length-side (Barnes et al. 2017) based on the cosmological parameters derived from the 2013 analysis of the Planck data ($H_0 = 100\,\mathrm{h} = 67.77\,\mathrm{km\,s^{-1}\,Mpc^{-1}}$, $\Omega_\Lambda = 0.693$, $\Omega_\mathrm{m} = 0.307$, $\Omega_\mathrm{b} = 0.04825$, $\sigma_8 = 0.8288$, $n_\mathrm{s} = 0.9611$, and $Y = 0.248$; Planck Collaboration et al. 2014). Despite the different cosmologies between our mass

[1] All published mass models based on the pre-HFF data by Coe, Bradley & Zitrin (2015), Johnson et al. (2014), and Richard et al. (2014) are publicly available at http://archive.stsci.edu/prepds/frontier/lensmodels/.

reconstruction and the simulation, the subhalo comparison analysis will not be affected as the differences between the two sets of cosmological parameters are not significant.

Dark matter haloes were selected using the friends-of-friends algorithm (Davis et al. 1985), and bound subhaloes were identified using the SUBFIND algorithm (Springel et al. 2001; Dolag et al. 2009). Thirty haloes at $z = 0$ were selected for the zoom-im realization taking into account a mass $M_{200} > 10^{14}\,\mathrm{M}_{\odot}$ and an isolation criterion (no other massive haloes within 20 times the R_{200} radius).

The EAGLE simulation code (Crain et al. 2015; Schaller et al. 2015; Schaye et al. 2015) is used to resimulate the halo selection sample assuming a mass of 9.7×10^6 and $1.8 \times 10^6\,\mathrm{M}_{\odot}$ for the dark matter and gas particles, respectively, a softening length of 2.66 comoving kpc for $z > 2.8$ and a physical softening length of 0.70 kpc for $z < 2.8$. Post-processed halo and subhalo catalogues were generated for all output redshifts using the SUBFIND algorithm. Simulated clusters attempt to reproduce the formation of rich galaxy clusters with a model that yields a galaxy population that is a good match to the observed field population.

4 GALAXY CATALOGUES

In this section, we detail the galaxy catalogues used for the lensing analysis and the optical luminosity distribution. We first present the source detection, photometry, and shape measurements performed in the optical stacked images described in Section 2. Then we discuss the background source identification. Cluster members are used to model the cluster gravitational potential and to obtain the optical light distribution. Background galaxies, defined as galaxies behind MACS J0416 and hence lensed by the cluster, are used to perform the weak-lensing analysis.

4.1 Source catalogue and shape measurements

In order to detect sources in the HFF images, and measure the shapes of background galaxies for the weak-lensing analysis, we use the ACS/*F*814*W* filter. As in J15, we follow the same approach as for the COSMOS survey (Leauthaud et al. 2007) when adapted to cluster fields (Jauzac et al. 2012). We compute the shapes using the pipeline PYRRG[2] developed by D. Harvey (Harvey et al. 2015, 2019) and based on the RRG method (Rhodes, Refregier & Groth 2000).

The source detection and the photometry are performed using the SEXTRACTOR package (Bertin & Arnouts 1996) applying the '*Cold–Hot*' method: (1) SEXTRACTOR is executed with a configuration optimized to detect only the brightest objects (*cold* step), and (2) SEXTRACTOR is run with a configuration optimized to detect faint objects (*hot* step). The two catalogues are then merged by including all objects detected during the *cold* step, plus the objects detected during the *hot* step but not the *cold* step. Finally, double detections are removed by discarding all objects within one FWHM_IMAGE of each other, keeping larger objects. The source classification as galaxies, stars, and false detections is performed according to the distribution of the objects in the MAG_AUTO versus peak surface brightness MU_MAX plane (see Leauthaud et al. 2007, for further details).

Galaxy shapes are computed using the RRG method (Rhodes et al. 2000). This method was specifically developed for weak-lensing analysis of space-based observations. Since the ACS point spread function (PSF) varies due to the telescope 'breathing', the effective focus of the observation is determined by comparing the ellipticity of the sources classified as stars with a grid of simulated PSF images generated by Rhodes et al. (2007). PSF parameters are interpolated first creating a grid of positions which covers the entire field of view (FOV) of the combined drizzled image. Then, for each position in the drizzled image, the PYRRG code identifies how many images cover this position and computes the PSF while rotating the moments such that they are in the reference frame of the stacked image. Finally, it averages the moments over the stack to obtain the PSF at the considered position.

From the RRG method, we obtain the galaxy moments corrected from instrumental effects. For each galaxy, the ellipticity, $e = (e_1, e_2)$, and the size, d, are computed as

$$e_1 = \frac{I_{xx} - I_{yy}}{I_{xx} + I_{yy}},$$

$$e_2 = \frac{2I_{xy}}{I_{xx} + I_{yy}},$$

$$d = \sqrt{\frac{I_{xx} + I_{yy}}{2}}, \quad (1)$$

where I_{ij} are the second-order Gaussian-weighted moments. The shear estimator, $\tilde{\gamma}$, is obtained from the measured ellipticities according to

$$\tilde{\gamma} = C\frac{e}{G}, \quad (2)$$

where G is the shear susceptibility and is computed following equation (28) in Rhodes et al. (2000), and C is the calibration factor ($C = 0.86$, see Leauthaud et al. 2007, for further details).

Finally, we only consider galaxies with $22.5 < m_{F814W}$ for our weak-lensing analysis. We also discard galaxies with shape measurements based on fewer than three exposures, in order to discard galaxies near the edges of the observed fields. We also set a threshold on the detection limit (FLUX_AUTO/FLUXERR_AUTO >4.5), the ellipticity parameter ($e < 1$), and the size ($3.6 < d < 30$ pixels).

4.2 Cluster members

The contribution of cluster galaxies must be carefully considered in the mass modelling based on strong lensing observations (Harvey, Kneib & Jauzac 2016). In this work, we perform a weak-lensing analysis combined with the best-fitting strong-lensing mass model from previous work (see Section 5) to model the projected mass density distribution in the outskirts of the cluster, where cluster member contributions to the total mass distribution are not significant. Therefore, the inclusion of interlopers in the cluster member sample has not a major impact on the mass modelling. Moreover, since these galaxies are considered for the background galaxy selection, we adopt a relax criterion for their identification.

We identify cluster members in each field following the criteria presented in J15, considering all the galaxies with $m_{F814W} < 23.4$. For both cluster and parallel fields, we identify cluster members as galaxies with photometric redshifts (z_{phot} members) that satisfy $0.35 < z_{\mathrm{phot}} < 0.44$, and those with spectroscopic redshifts (z_{sepc} members) that satisfy $|z_{\mathrm{cluster}} - z_{\mathrm{spec}}| < 0.0104$, with $z_{\mathrm{cluster}} = 0.3979$. We also include galaxies that fall within 3σ of the cluster red sequence in both ($m_{F606W} - m_{F814W}$) versus m_{F814W} and ($m_{F435W} - m_{F606W}$) versus m_{F814W} colour–magnitude diagrams (red-sequence members). We model the red sequence with a Gaussian function, fitting the colour–magnitude distribution of galaxies with m_{F814W}

[2] https://github.com/davidharvey1986/pyRRG.

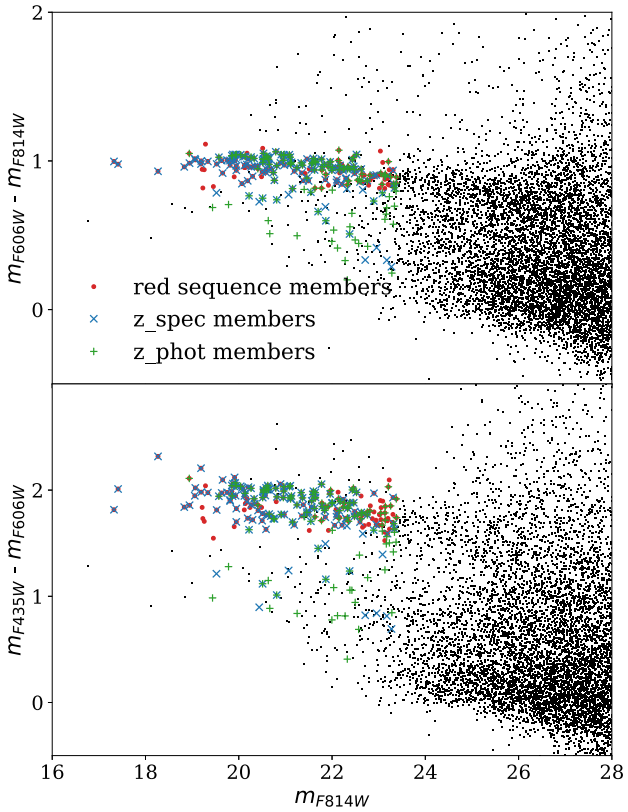

Figure 1. Colour–magnitude diagrams for all galaxies within the cluster and the parallel fields. Red-sequence galaxies are selected according to a Gaussian fit, including all the galaxies within 3σ, and are marked as red dots. Galaxies selected according to their photometric and spectroscopic redshifts are marked as blue crosses and green pluses, respectively.

> 22. In spite this being a rough selection which can lead to the inclusion of non-cluster members (Connor et al. 2019), all these galaxies are taken into account in order to place more conservative boundaries for the background galaxy selection. The mean colour of the best-fitting Gaussian is 0.99 (1.92) with a standard deviation colour of 0.06 (0.14) for the galaxies in the cluster (parallel) field. In total, we identify 245 galaxies as cluster members. In Fig. 1, we show both colour–magnitude diagrams with the selected members marked.

4.3 Background galaxies

We select background galaxies, defined as galaxies behind the cluster and lensed by it, following J15. We take into account the position of the sources classified as galaxies in the colour–colour space.

For galaxies with either spectroscopic or photometric redshifts, we classify them as foreground galaxies if $dz < |z_{\rm cluster} - z_{\rm spec}$ (where $dz = 0.0104$) and $z_{\rm phot} < 0.35$. According to this classification and considering cluster members identified previously, we identify a region in the colour–colour space defined as

$$(m_{F435W} - m_{F606W}) > 0.3,$$

$$(m_{F435W} - m_{F606W}) < 0.67776,\ (m_{F435W} - m_{F814W}) + 0.2,$$

$$(m_{F435W} - m_{F606W}) > 0.87776,\ (m_{F435W} - m_{F814W}) - 0.86.$$

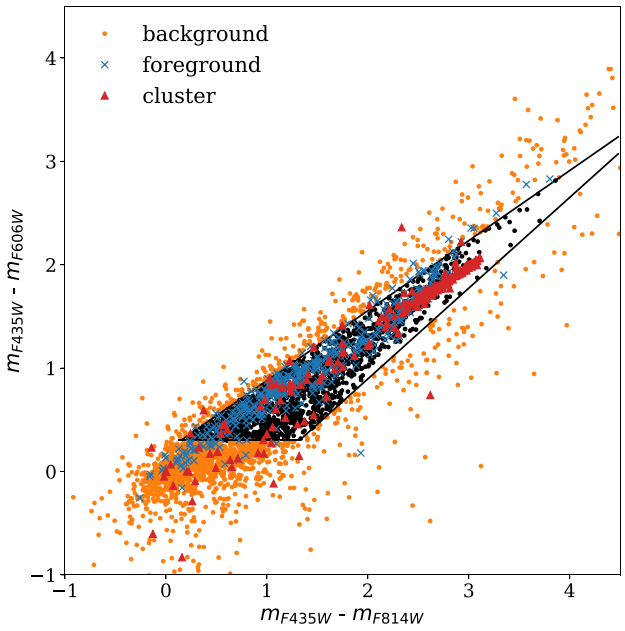

Figure 2. Colour–colour diagram for all galaxies detected within the cluster and the parallel fields. Galaxies classified as foreground and cluster members are marked with crosses and triangles, respectively. Black lines mark the background galaxy selection region. Galaxies outside that region are considered as background objects (orange points).

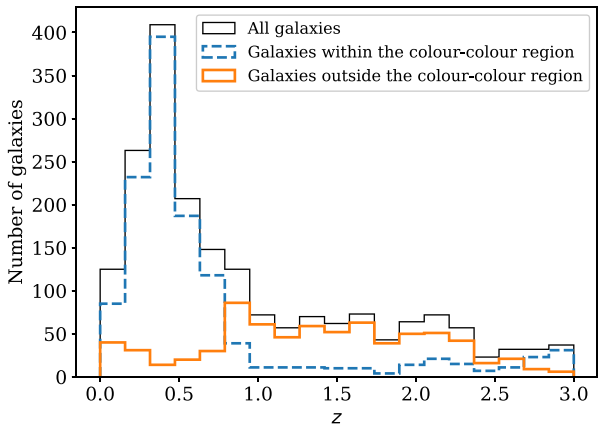

Figure 3. Redshift distribution of all galaxies that have photometric or spectroscopic redshifts (solid line). The dashed histogram and the thicker line histogram show the distribution of galaxies within and outside the colour–colour region defined for the background galaxy selection.

All galaxies within this region are considered as either foreground or cluster objects. They are thus removed from our final weak-lensing catalogue together with galaxies at $z_{\rm phot} > 3$ (see Fig. 2). In Fig. 3, we show the redshift distribution for the subset of galaxies with redshift information that lie within and outside the defined colour–colour region. Approximately $\sim$89 per cent of the unlensed galaxies (foreground and cluster) are discarded using this colour–colour criterion.

We classify 1684 sources as background galaxies, 549 of which have redshift information. With this selection criteria, we obtain a background galaxy density of $\sim$70 and $\sim$50 galaxies arcmin^{-2} for the cluster and parallel field, respectively. These differences in the

observed galaxy density are mainly due to the shorter exposure for the frames observed in the parallel field (see Table 1) as well as for the larger density of member galaxies in the cluster field that hamper the detection of fainter sources.

To model the redshift distribution for the galaxies without redshift information, we use the following function:

$$N(z) = z^{\alpha} \exp -(z/z_0)^{\beta}. \quad (3)$$

We fix $\alpha = 2$, and fit the redshift distribution of the background galaxies with redshift information, obtaining $z_0 = 1.28$ and $\beta = 1.82$. This distribution aims to mimic the whole sample redshift distribution, allowing to take into account redhsift values lower than the cluster redshift itself, and thus considering the dilution introduced by the contamination from foreground galaxies.

5 MASS MODELLING

We model the mass distribution using a grid-based model combined with a parametric model following a similar approach as in J15. The grid-based model consists of a set of radial basis functions (RBFs) located at the nodes of the multiscale grid (Jullo & Kneib 2009; Jullo et al. 2014). Each RBF is modelled with a dual pseudo-isothermal elliptical mass distribution (dPIE; Elíasdóttir et al. 2007). This profile is a two-component pseudo-isothermal mass distribution with a core radius ($r_{\rm core}$, defined as the distance between an RBF and its closest neighbour) and a scale radius ($r_{\rm cut}$, assumed to be three times $r_{\rm core}$, Jullo & Kneib 2009). During the fitting procedure only the potential amplitudes vary according to the lensing signal and hence, follows the projected density distribution. We use a uniform grid of the same size as the FOV. The resolution of the grid is given by the core radius parameter, $r_{\rm core}$, which also could be understood as a softness parameter.

We select this parameter considering the computed signal-to-noise ratio (S/N) maps. We tried three different grid resolutions, 3.0, 4.5 and 6.0 arcsec for the cluster field and 6.0, 7.5, and 9.0 arcsec for the parallel field, since a lower signal is expected for this field. No significant differences were obtained in the resultant mass density distributions derived for the different resolutions considered. Nevertheless, we fix $r_{\rm core}$ at 6 arcsec and 9 arcsec for the cluster and parallel fields, respectively, since for larger resolutions the obtained distributions show clumpy structures with S/N lower than 3. On the other hand, for the main field lower resolution grid, substructures detected in the surface density map at a high significance (S/N $>$ 5) are merged. At this resolution, the obtained grids consist of 1200 and 770 nodes for the cluster and parallel field, respectively.

For the cluster field, we combine the grid with two cluster-scale dark matter haloes and 219 cluster members in the inner core, optimized using strong-lensing constraints. These two dark matter haloes are modelled with pseudo-isothermal elliptical mass distributions (PIEMD; Elíasdóttir et al. 2007), according to the results from the strong-lensing analysis presented in Jauzac et al. (2014; Table 2).

On the other hand, the parallel field does not include large-scale dark matter haloes as in the core. We only include the 26 cluster members galaxies identified as described in Section 4.2. Those are also modelled with dPIE potentials with parameters fixed according to J15: $m^* = 19.76$, $\sigma^* = 119\,{\rm km\,s^{-1}}$, and $r^*_{cut} = 85\,{\rm kpc}$. Although these parameters are derived for galaxy members close to the cluster core, we do not expect significant differences in the derived surface density mass.

While the parametric model used to trace the core projected density distribution is fixed to the best-fitting obtained by J14, the RBFs are optimized using the weak-lensing constraints identified in Section 4 in both fields individually. According to the selection described in Section 4.3, we use 984 and 700 background galaxies for the cluster and parallel fields, respectively. To implement this fitting procedure, we use LENSTOOL[3] (Jullo et al. 2007) which includes a Bayesian optimization based on http://www.inference.org.uk/bayesys/. The projected mass for each field is obtained by averaging the results of the 200 iterations, and errors are based on the standard deviation of the derived maps.

Table 2. Pseudo-isothermal elliptical mass distribution parameters used as input for the two cluster-scale dark matter haloes modelling. These were obtained according to the strong-lensing analysis presented in J15. The corresponding parameters describe the two cluster scale halo components (C1 and C2) of the cluster.

Component	C1	C2
RA (J2000)	04:16:09.4	04:16:07.5
Dec. (J2000)	− 24:04:01.4	− 24:04:47.4
e	0.7	0.7
θ	148.0	127.4
$r_{\rm core}$ (kpc)	77.8	103.3
r_{cut}(kpc)	1000	1000
σ (km s^{-1})	779	955

6 RESULTS

In this section, we present the derived projected surface density maps reconstructed from the lensing analysis and compare it with the optical and X-ray luminosity distribution. In order to do that, we compute the optical luminosity maps of both the cluster and the parallel fields by pixellating the FOV and adding the brightness of the enclosed cluster members in each pixel. For this, we compute the brightness according to their magnitude in the $F814W$ passband, m_{F814W}. We then smooth the brightness map using a Gaussian kernel with a standard deviation of 7.56 and 27 arcsec for the cluster and the parallel fields, respectively. Brightness and projected mass contours are obtained using SAOIMAGE DS9.[4]

According to the surface mass density maps obtained with our lensing reconstruction, we detect five overdensities with significance $>5\sigma$ in the cluster and parallel fields, i.e. five times the median S/N in an aperture of 10 arcsec centred on each detected overdensity. In Table 3, we describe the properties of all the substructures detected in this work within the cluster and the parallel fields, together with the substructures detected in the cluster field by J15. To discard that detected substructures are produced by outliers in the background galaxy sample with less reliable shear measurements or by the inclusion of artefacts with abnormally high ellipticity, we recompute the surface mass density maps but randomly discarding 10 per cent of the background galaxies. We perform 100 realizations for both the cluster and parallel fields. We then measure the mass in fixed apertures at the locations of the substructures. The distributions of the computed masses for each of them are normaly behaved with a dispersion comparable to the estimated errors presented in Table 3. Therefore, we discard that the detected overdensities can be produced by outliers in the galaxy sample.

[3] https://projets.lam.fr/projects/lenstool/wiki.
[4] http://ds9.si.edu/site/Home.html.

Table 3. Properties of the detected overdensities within the main and the parallel fields. S1 and S2 are the overdensities detected and described by J15. S1c, S2c, S3c, and S4c are the substructures detected in this work in the cluster field and S1p is the substructure detected in the parallel field. Masses are in units of $10^{13}\,h_{70}^{-1}\,\mathrm{M}_{\odot}$. The overdensities between parenthesis have neither optical nor X-ray detected counterpart, hence, a deep study is needed to confirm their detection.

ID	RA (J2000)	Dec. (J2000)	$M\,(R<100\,\mathrm{kpc})$	$M\,(R<200\,\mathrm{kpc})$	σ	D_{G1-S} (kpc)
S1	4:16:03.970	−24:05:41.66	4.2 ± 0.6	–	7.5	650
S2	4:16:14.633	−24:03:49.09	1.5 ± 0.2	–	7.3	409
S1c	4:16:02.770	−24:03:49.09	3.7 ± 0.6	11.1 ± 1.5	5.8	687
S2c	4:16:03.885	−24:04:33.48	3.6 ± 0.4	12.5 ± 1.3	8.4	418
(S3c)	4:16:07.571	−24:02:56.10	2.8 ± 0.3	8.6 ± 1.2	8.7	376
(S4c)	4:16:14.746	−24:03:13.96	3.5 ± 0.5	11.3 ± 2.1	7.0	487
S1p	4:16:32.207	−24:05:18.33	2.1 ± 0.4	5.0 ± 1.1	6.3	1737

In the next subsections, we discuss the results for the cluster and parallel field separately, comparing our mass estimations with previous analysis.

6.1 Cluster field

In Fig. 4, we show the composite colour *HST*/ACS images in the *F*814*W*, *F*606*W*, and *F*435*W* pass-bands together with the surface mass density (solid lines) and brightness contours (dashed lines) for the cluster field. Surface density contours are linearly spaced, obtained from (1.17×10^{9}) up to $(2.93\times10^{9})\,h_{70}^{-1}\,\mathrm{M}_{\odot}\,\mathrm{kpc}^{-2}$. Brightness contours are obtained from $m_{F814W}=23.3$ up to $m_{F814W}=20.0$. There is a good agreement between the projected mass and the brightness distributions.

We derive projected masses within circular apertures centred at the brightest galaxy member location (G1: RA (J2000) = 4:16:09.144, Dec. (J2000) = −24:04:02.94) considering different aperture radii in order to compare our results with previous mass determinations. Taking into account an aperture of $R<200\,\mathrm{kpc}$, we obtain $M(R<200\,\mathrm{kpc})=(1.93\pm0.07)\times10^{14}\,h_{70}^{-1}\,\mathrm{M}_{\odot}$. This value is higher than other previous mass determinations as $(1.63\pm0.03)\times10^{14}\,h_{70}^{-1}\,\mathrm{M}_{\odot}$, $(1.66\pm0.05)\times10^{14}\,h_{70}^{-1}\,\mathrm{M}_{\odot}$ and between 1.72 and $1.77\times10^{14}\,h_{70}^{-1}\,\mathrm{M}_{\odot}$ obtained by Richard et al. (2014), J15, and Grillo et al. (2015), respectively. We obtain $M(R<250\,\mathrm{kpc})=(2.71\pm0.12)\times10^{14}\,h_{70}^{-1}\,\mathrm{M}_{\odot}$, which is also higher than what has been reported by other authors: between 2.35 and $2.43\times10^{14}\,h_{70}^{-1}\,\mathrm{M}_{\odot}$ according to Grillo et al. (2015) and significantly higher than the reported masses by Johnson et al. (2014) and Gruen et al. (2014) of $(1.8\pm0.3)\times10^{14}$ and $(1.77^{+0.31}_{-0.13})\times10^{14}\,h_{70}^{-1}\,\mathrm{M}_{\odot}$, respectively. Finally, we obtain $M(R<320\,\mathrm{kpc})=(3.92\pm0.22)\times10^{14}\,h_{70}^{-1}\,\mathrm{M}_{\odot}$, higher than the reported values by Jauzac et al. (2014, 2015a) and Grillo et al. (2015). As stated by Grillo et al. (2015), differences in these mass estimates could be caused by displacements in the adopted cluster mass centres, details of the lensing models, and/or the degeneracy between the mass of a lens and the redshift of a multiply imaged source. Also, in contrast to the results obtained in J15, the inclusion of weak-lensing information in this work led to larger mass estimates. In this case differences cannot be addressed by displacements in the adopted centre. To check our modelling, we compare our mass estimate using only strong-lensing constraints, i.e. without the grid modelling, with the mass derived by Jauzac et al. (2014), obtaining a perfect agreement. Therefore, discrepancies are introduced when optimizing weak-lensing constraints. We suspect that the observed discrepancies are due to the new redshift information included in this work.

J15 identified two mass overdensities close to the cluster, S1 and S2, which are marked in Fig. 4, and described in Table 3. S1 is also confirmed by the presence of a galaxy overdensity in this region coincident with a peak in the light distribution. Although there is no X-ray emission excess confirmed in this region, the overall cluster emission is elongated in the direction of both mass structures of the cluster core (Ogrean et al. 2015). Moreover, if the substructures have already merged with the cluster haloes, the dark matter could be decoupled from the gas and, therefore, a X-ray remnant core would not be expected. This scenario is also supported for S1 since Ogrean et al. (2015) reported a density discontinuity close to this substructure that could be originated by a previous interaction between one of the main halo components, C2, and S1.

In this work, we detect four mass peaks in the cluster field, labelled as S1c, S2c, S3c, and S4c. These are marked in Fig. 4 and their properties are detailed in Table 3. S1c and S2c are located close to galaxy overdensities which support their detection in our lensing analysis and can be considered as cluster substructures. Also, S1c is located close to S1, and has a projected mass of $M(R<100\,\mathrm{kpc})=(3.74\pm0.64)\times10^{13}\,h_{70}^{-1}\,\mathrm{M}_{\odot}$, which is in agreement with the J15 estimate for S1 ($M(R<100\,\mathrm{kpc})=(4.22\pm0.56)\times10^{13}\,h_{70}^{-1}\,\mathrm{M}_{\odot}$). Moreover, there is an excess in the X-ray emission close to the location of S2c that can be observed in the X-ray map presented by Ogrean et al. (2015) (see fig. 8 in Ogrean et al. 2015). On the other hand, S3c has no counterpart in the brightness map. Nevertheless, it is detected with high significance and could possibly correspond to a dark matter halo that already interacted with the cluster. To test if the detected peaks are not caused by the modelling considerations, we compute the projected surface density maps using only the grid and neglecting the parametric contribution of the two main haloes and the galaxy members. Considering this analysis, we do not detect significant signal close to S3c and S4c locations, therefore these peaks can be produced by the imposition of the parametric model on the lensing data. We also perform a quick test by obtaining the surface distribution using the reconstruction method developed by Kaiser & Squires (1993). With this analysis, we obtain a significant density distribution at the two main halo locations, C1 and C2, and close to Sc1 and Sc2. Further inspection about how the modelling can impact the detection of substructures, which is out of the scope of this paper, needs to be performed in order to assess for these discrepancies.

There is no significant signal close to the location of S2. Nevertheless, if we lower the threshold in the mass contours, we can detect an overdensity close to this substructure but with a detection significance threshold lower than 5σ. This is comparable with the detection level of some artefacts detected close to the edge

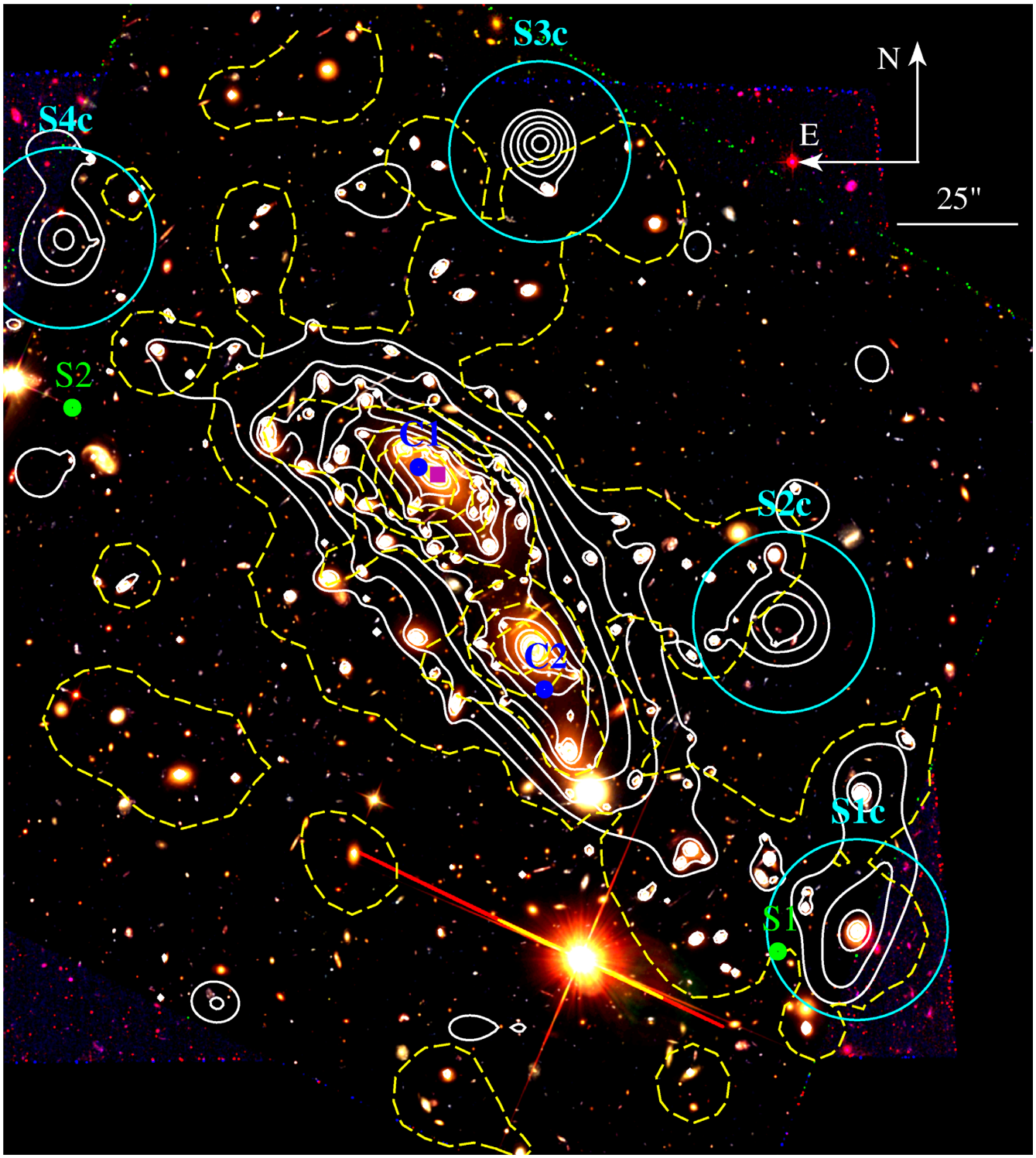

Figure 4. Composite colour *HST*/ACS image using the *F*814*W*, *F*606*W*, and *F*435*W* pass-bands, together with the projected mass (white solid line) and brightness contours (yellow dashed line) for the cluster field overlaid. Projected surface mass density contours are linearly spaced, obtained from (1.17×10^9) up to $(2.93 \times 10^9)\, h_{70}^{-1}\, \mathrm{M}_\odot\, \mathrm{kpc}^{-2}$. Brightness contours are obtained from $m_{F814W} = 23.3$ up to $m_{F814W} = 20.0$. We also mark the brightest galaxy member location (G1, purple square) centres of the fixed halo components (C1 and C2), the detected substructures (S1 and S2) by J15 and the detected substructure in this work, labelled as S1c, S2c, S3c, and S4c. The size of the rings that enclose the substructures correspond to 100 kpc at the cluster redshift.

of the field. Edge effects significantly hamper the identification of substructures in these regions. Errors in surface density maps start to significantly increase at distances larger than $\sim$350 kpc, with the median error at the edges (350–550 kpc) more than two times higher than in the central region of the cluster field. Such discrepancies could be addressed by the BUFFALO survey (GO-15117; PIs: Steinhardt & Jauzac) which images the surrounding area of the HFF cluster field of MACS J0416.

In Fig. 5, we show the surface density profile computed using the projected lensing mass map for the cluster field, and centred on the brightest galaxy member, G1. Given that the uncertainties in the estimated lensing signal are expected to be dominated by shape noise, we do not expect a noticeable covariance between adjacent radial bins. Therefore, errors are computed in each bin, averaging the standard deviation map, and treating them as independent. We also compute profiles centred in G1 but restricting the field to a triangular wedge aperture of 10 deg with their apex located at G1 and pointing in the direction of each detected substructure. As one can see, the presence of these overdensities can be detected in the profiles as peaks located at their respective distances from G1, D_{G1-S}, detailed in Table 3.

6.2 Parallel field

Fig. 6 shows the composite colour *HST*/ACS image using the *F*814*W*, *F*606*W*, and *F*435*W* pass-bands together with the projected mass and brightness contours for the parallel field. Projected surface mass density contours are linearly spaced, obtained from (4.69×10^8) to $(1.64 \times 10^9)\, h_{70}^{-1}\, \mathrm{M}_\odot\, \mathrm{kpc}^{-2}$. Brightness contours are obtained from $m_{F814W} = 23.3$ to $m_{F814W} = 20.8$. There is a general agreement between the projected mass and the brightness distributions particularly considering that the brightness map is poorly determined since it is based on only 26 cluster galaxies.

The overall projected surface mass density is consistent with a clumpy distribution connected by filament-like structures to the cluster core. In this field, we detect one mass peak, S1p, located at RA (J2000) = 4:16:32.207, Dec. (J2000) = −24:05:18.327, and with a projected mass within a 100 kpc aperture of $(2.1 \pm 0.4) \times 10^{13}\, h_{70}^{-1}\, \mathrm{M}_\odot$. This is coincident with a peak in the brightness distribution, as well as with a galaxy overdensity. It appears to be a good correlation between the elongation of the projected mass distribution and the direction pointing to the cluster. In particular, two of the overdensities are aligned with the direction of S4c and G1 as marked in Fig. 4.

The detected structures do not have evident counterparts in the *Chandra* image of the field. We used PYPROFFIT[5] (Eckert, Molendi & Paltani 2011) to extract X-ray surface brightness profiles around the position of S1p. The X-ray signal is consistent with the background level. Assuming that the S1p is real and located at the redshift of the cluster, we can thus set an upper limit on the X-ray luminosity of 4.1×10^{41} erg s^{-1} ([0.5–2] keV rest frame, 90 per cent confidence level) within a circle of 1 arcmin radius around the source. However, we find a low-significance excess of X-ray emission located ∼0.7 arcmin from S1p, close to the arrow that points towards S4c in Fig. 6. The tentative X-ray source is centred on RA (J2000) = 4:16:29.646, Dec. = −24:05:44.044. We also extracted the brightness profile around this position, which confirms a 2.9σ excess above the background. Again assuming that the source is located at the redshift of MACS J0416, we derive a luminosity of $(8.3 + /2.9) \times 10^{41}$ erg s^{-1} in the [0.5–2] keV band (rest frame) within 1 arcmin radius. If the emission originates from a virialized infalling halo that has not yet interacted with MACS J0416, such a luminosity would be typical of a galaxy group with $kT \sim 0.8$ keV and $M_{500c} \sim 2 \times 10^{13}$ $\mathrm{M}_\odot$ according to the scaling relations of Giles et al. (2016) and Lieu et al. (2016). Conversely, if S1p is confirmed to be a real substructure and given its substantially larger lensing mass, it would be almost entirely depleted of hot gas. This would imply that the surrounding dark matter halo has survived a previous interaction with the main cluster, whereas the gas content has been almost entirely stripped. According to the X-ray surface brightness profile of the main halo component C1, the core is composed of a very compact core and a more extended gas halo which suggest a possible previous merger event (Ogrean et al. 2015) which would favour this scenario.

[5]https://github.com/domeckert/pyproffit.

6.3 Substructure analysis

According to the projected density distribution derived from the lensing analysis, we detect up to 5 mass peaks with $M(R < 200\,\mathrm{kpc}) > 5 \times 10^{13}\, h_{70}^{-1}\, \mathrm{M}_\odot$. The properties of massive substructures detected in massive galaxy clusters can be used as a test for ΛCDM, by comparing the observed detections with the subhalo mass function predicted by numerical simulations (e.g. Natarajan et al. 2007; Grillo et al. 2015; Munari et al. 2016; Schwinn et al. 2017). In order to do the comparison we select one cluster, with similar properties as MACS J0416, from the 30 Hydrangea/C-EAGLE simulated galaxy clusters described in Section 3 and compare our lensing results with the subhalo distribution of the selected cluster within a projected 2D plane.

The selected simulated cluster is located at $z = 0.411$ with a $M_{200} = 7.2 \times 10^{14}\, \mathrm{M}_\odot$ (Cluster ID: CE-28, according to table A1 in Barnes et al. 2017). This corresponds to projected aperture masses: $M(R < 200\,\mathrm{kpc}) = 1.5 \times 10^{14}\, \mathrm{M}_\odot$, $M(R < 250\,\mathrm{kpc}) = 1.9 \times 10^{14}\, \mathrm{M}_\odot$, and $M(R < 320\,\mathrm{kpc}) = 2.50 \times 10^{14}\, \mathrm{M}_\odot$. In order to identify subhaloes[6] in the field that would be detected in our lensing analysis, we first select objects from the subhalo catalogue within a 3 Mpc radius, excluding a central region of 350 kpc to mimic the lack of sensitivity to dense structures due to the presence of the dense core. Then we project their centres into the sky plane within ±5 Mpc, and compute the projected masses enclosed by circular apertures of 200 kpc radius. Detected subhaloes are marked in Fig. 7 together with the projected mass map of the simulated cluster. We only detect one subhalo with an aperture mass $> 5 \times 10^{13}\, \mathrm{M}_\odot$, which is the expected detection threshold in our lensing analysis. This subhalo, labelled as 2 in Fig. 7, has an aperture mass of $5.7 \times 10^{13}\, \mathrm{M}_\odot$ and is located at 1703 kpc from the cluster centre, at a similar distance as the mass peak reported in the parallel field, S1p. However, the selected parallel field is located perpendicular to the mass distribution while the subhalo is located in a direction close to the cluster elongation.

It is important to consider that the HFF fields only represent ∼20 per cent of the area considered for the identification of subhaloes in the simulated cluster. Moreover, the observed region is only continuous out to ∼800 kpc from the cluster centre, where four of the five reported substructures are located. Within this region, we identify six subhaloes in the simulated cluster, with an average mass $\langle M(R < 200\,\mathrm{kpc})\rangle = 2 \times 10^{13}\, \mathrm{M}_\odot$, the most massive one located at 600 kpc from the centre with $M(R < 200\,\mathrm{kpc}) = 3.1 \times 10^{13}\, \mathrm{M}_\odot$. Therefore, we can argue that there are significant differences between the subhalo distribution observed in the simulated cluster and the one observed in MACSJ 0416. Since the simulated cluster appears to be relatively dynamically relaxed, and was observed as an isolated halo, it is sensible to think we are in the case of a more evolved system than MACS J0416 itself. MACS J0416 is a very elongated cluster, showing an obvious bimodal density mass

[6]Here, we refer to all identified haloes within the considered region as subhaloes, even if they are not included within the main halo of the simulated cluster.

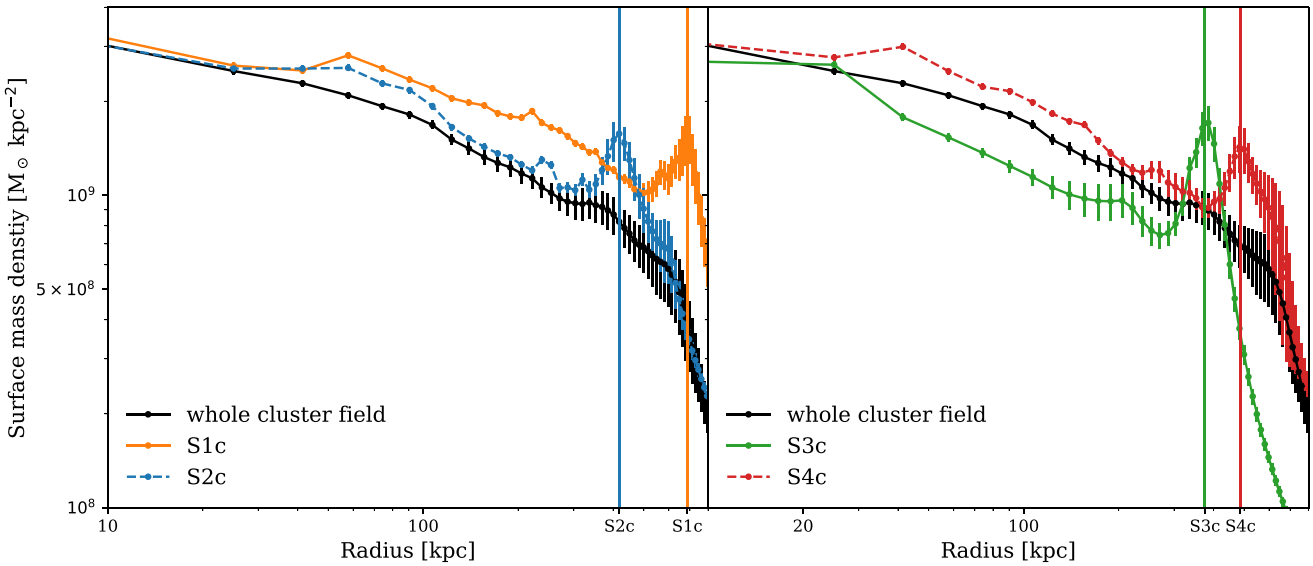

Figure 5. Surface mass density profiles obtained for the complete cluster field (solid line). Dashed lighter lines show the profiles computed within a triangular wedge region, defined with an amplitude of 10 deg with their apex located at G1 and pointing to S1c and S2c substructure (left-hand panel) and to S3c and S4c (right-hand panel). Substructures are detected as an excess in the surface mass density at the locations of each overdensity.

distribution. Taking into account that subhaloes tend to fall in the inner cluster regions at lower redshifts, the simulated cluster could be representing the next evolutionary stage of MACS J0416 in which the closest subhaloes have already merged with the cluster core. Discrepancies between the observed radial distribution of subhaloes and the one simulated were already reported by Natarajan et al. (2017). One reason could be that the selected simulated cluster is not representative of MACS J0416. HFF clusters were selected for their strong magnifying power, which biases the selection towards dynamically complex and extremely massive systems.

It is worth noting that three of the reported MACSJ 0416 substructures in this work are located close to the edges of the HFF FOV. This can significantly hamper the mass estimates of the detected substructures. The BUFFALO survey will triple the observed area, providing an almost continuous region between the cluster and the parallel fields (Fig. 8). It would thus provide a major improvement in the aperture masses estimates. Although the observed depth will be lower than the HFF observations (the exposure time for HFF is around 140 *HST* orbits while for BUFFALO is going to be of 4, corresponding to a total exposure time of 283 920 s against 560 s), BUFFALO is expected to detect the substructures reported in the cluster field and, therefore, to better characterize their physical properties.

7 SUMMARY AND CONCLUSION

In this work, we present the analysis of the matter distribution in the HFF massive galaxy cluster, MACS J0416. The analysis includes an optical analysis of the cluster core (cluster field), as well as its adjacent HFF 'blank' field (parallel field) combined with an X-ray study. This work is motivated by the upcoming observations from the BUFFALO survey, which will complete the region between the analysed fields.

We derive the projected surface mass density obtained from our lensing analysis, and compare our results with the optical and X-ray emission distributions. For both fields there is a good agreement between the projected density distribution and the optical emission. The resulting total masses computed within circular apertures centred on the brightest galaxy member of the cluster are higher than previous determinations (Gruen et al. 2014; Jauzac et al. 2014, 2015a; Johnson et al. 2014; Richard et al. 2014; Grillo et al. 2015). Discrepancies in these mass estimates and derived projected mass density distributions could be due to the different data sets, the different assumptions used by different lensing mass modelling algorithms, and the fact that the mass-sheet degeneracy is only partially broken by the inclusion of photometric redshifts (Grillo et al. 2015). Meneghetti et al. (2017) compared different lens modelling techniques to derive magnification estimates for the same clusters, and obtained very good agreements between the different techniques. Moreover, derived magnification maps by different authors led to similar parameters to calibrate the luminosity function (Ishigaki et al. 2018). This shows that the obtained overall projected mass density distribution is in good agreement with previous analyses. Also, Remolina González, Sharon & Mahler (2018) evaluate the predictive power of strong lensing models for MACS J0416, obtaining a good agreement in the arc prediction of the considered models. Although lensing modelling techniques have proven to be accurate for reconstructing projected density distributions, analyses based on different data sets, which include different redshift information, can lead to discrepancies in mass estimates. Therefore, more accurate error estimates that take into account these potential biases can be important in order to derive total masses values. A detailed study showing the comparison of derived aperture masses for different mass modelling techniques, and considering the impact of the redshift information of the weakly-lensed galaxies, could be valuable for a better understanding of the observed discrepancies. Niemiec et al. (2020) showed that when the mass reconstruction is performed using a sequential fit (first optimizing the parametric model in the cluster core with the strong-lensing constraints and then optimizing the grid model with weak-lensing constraints) as in this work, instead of a joint-analysis (optimizing using both strong and weak-lensing constraints

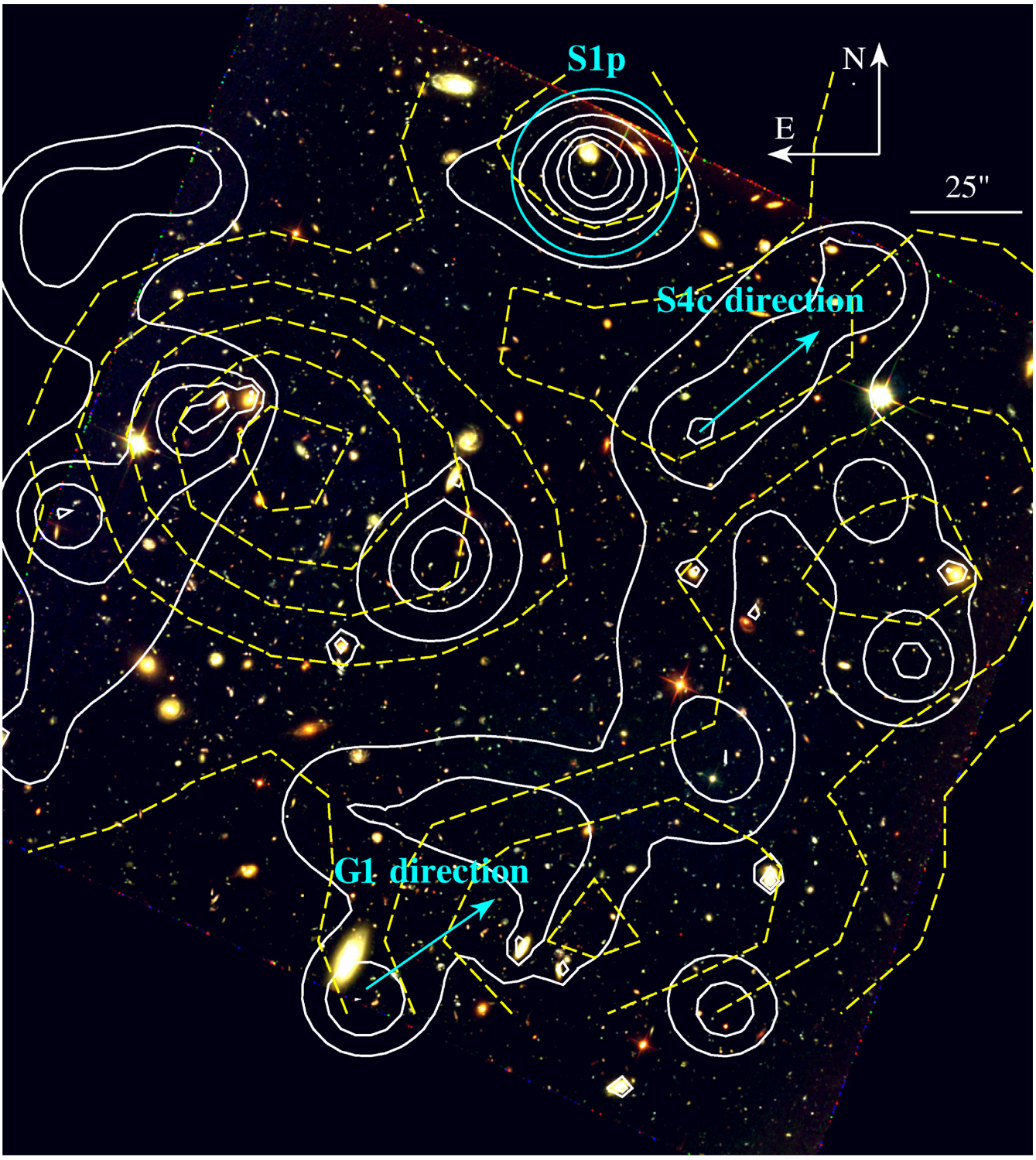

Figure 6. Composite colour *HST*/ACS image using the *F*814*W*, *F*606*W*, and *F*435*W* pass-bands, together with the projected mass (white solid line) and brightness contours (yellow dashed line) for the parallel field. Projected surface mass density contours are linearly spaced, obtained from (4.69×10^8) up to $(1.64 \times 10^9)\, h_{70}^{-1}\, \mathrm{M}_\odot\, \mathrm{kpc}^{-2}$. Brightness contours are obtained from $m_{F814W} = 23.3$ up to $m_{F814W} = 20.8$. We mark the substructure detected in this work, S1p. The arrows indicate the directions to G1 and S4c.

simultaneously), masses can be overestimated. This could explain the discrepancies observed with other authors except for the one presented in J15, where a sequential fit is also used to reconstruct the mass distribution.

We identify five mass peaks in both fields at the $>5\sigma$ level. Four of them are located in the cluster field with one of them matching a detection previously reported by J15. The identified peaks are also detected in the surface density profiles, when they are

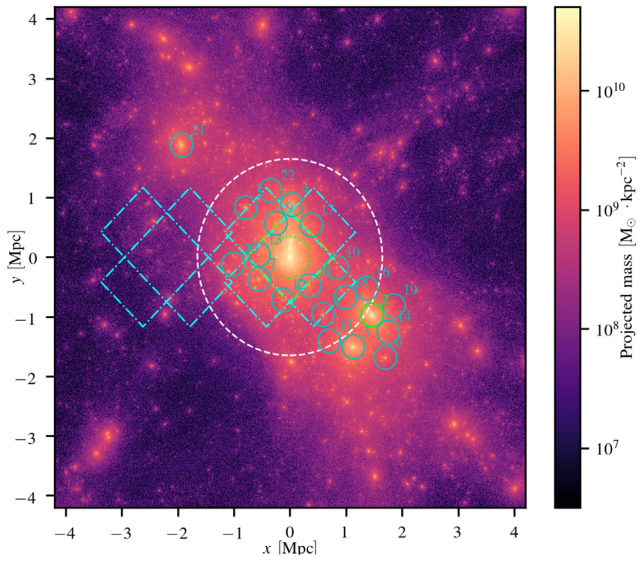

Figure 7. Projected mass map (using a logarithmic scale) of the selected simulated cluster at $z = 0.411$ with a $M_{200} = 7.43 \times 10^{14}\,M_{\odot}$ and a spherical overdensity radius $R_{200} = 1.64$ Mpc (dashed circle). The small cyan circles indicate the identified subhaloes. Green circle labelled as 2, corresponds to the only subhalo with an aperture mass $> 5 \times 10^{13}\,M_{\odot}$, which is the expected detection threshold in our lensing analysis. The dotted circle of 350 kpc radius corresponds to the central excluded region (see text for further details). Cyan dot–dashed line is a representation for BUFFALO FOV.

computed in triangular regions pointing to each of them. Three of the detected peaks, S1c, S2c, and S1p, lie close to galaxy overdensities which reinforces their identification and can be considered as substructures. Moreover, S2c is located close to an excess in the X-ray emission according to the map presented by Ogrean et al. (2015). In the case of S3c and S4c, we suspect that these structures can be generated by the imposition of the parametric model in the mass modelling, since they are not detected if we only use the grid modelling for the surface projected mass reconstruction.

For the parallel field, we obtain a clumpy projected mass distribution connected by filament-like structures. The overall projected mass distribution shows a potential alignment with the cluster direction, since two of the overdensities are elongated pointing to the brightest member galaxy and to one of the detected substructures in the cluster field. This is a key result because this field was selected expecting no significant mass distribution associated with the cluster. The detected substructure in this field, S1p, has no evident X-ray counterpart. The lensing mass estimated for this structure might suggest that it previously interacted with MACS J0416 and, as a result of this interaction, almost the whole gas content was stripped away. In this scenario, the detected low-significance excess of X-ray emission at ∼0.7 arcmin from S1p could be associated with the stripped gas as previously observed in other galaxy systems at low redshift (eg. Eckert et al. 2017). Nevertheless, this scenario should be less common without a remnant core. It is important to take into account that S1p is close to the edge of the FOV, thus border issues can considerably hamper the determination of the substructure physical properties such as the aperture mass and exact location. Further studies based on BUFFALO observations can confirm the presence of this structure and reinforce the striping scenario.

In order to test our results and make further predictions for the BUFFALO survey, we compare the distribution of substructures in MACS J0416 with the one observed in a Hydrangea/C-EAGLE simulated cluster. We identify 21 subhaloes within a 3.0 Mpc radius from the cluster centre. Only one of these subhaloes has an aperture mass $M(R < 200\,\mathrm{kpc}) > 5 \times 10^{13}\,M_{\odot}$, which is the expected threshold according to our lensing analysis. This subhalo is located at a projected distance from the cluster centre that is in agreement with the location of S1p, but in a direction close to the simulated cluster elongation. In the inner region (<800 kpc) of the simulated cluster, where we report four substructures for MACS J0416, none of the

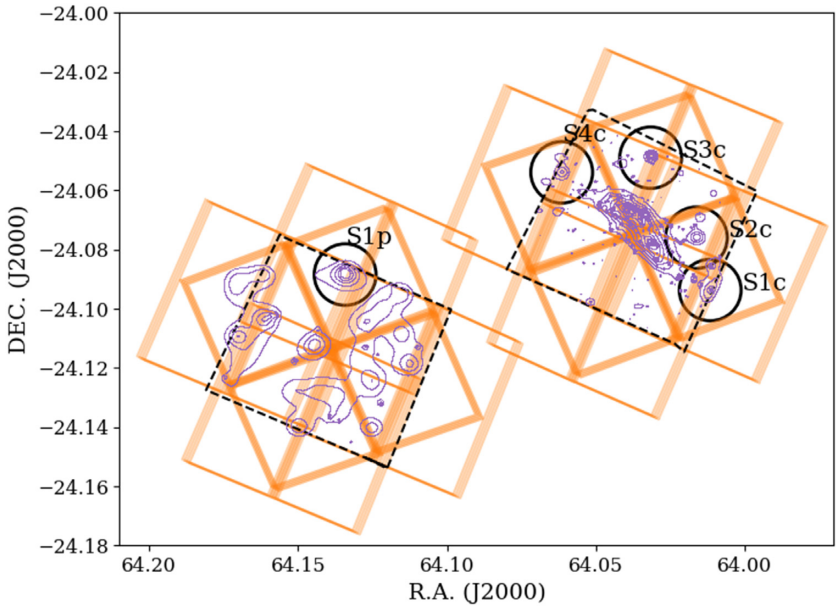

Figure 8. Substructure locations within the HFF (dashed black lines) and BUFFALO (orange lines) footprints. The circles correspond to an aperture of 200 kpc radius. Contours correspond to the derived projected density distributions in the parallel and cluster field. It is worth noting that these contours are obtained at different density levels as specified in Fig. 4 and 6.

identified subhaloes satisfy the lensing aperture mass threshold, with the most massive identified subhalo within this region having $M(R < 200\,\mathrm{kpc}) = 3.1 \times 10^{13}\,\mathrm{M}_{\odot}$. Therefore, we conclude that the simulated cluster represents a dynamically more evolved system in which all of the subhaloes close to the core have already merged with the cluster. Discrepancies in the radial distribution of subhaloes may be due to the fact that the simulated cluster does not adequately reproduce the observational properties of the HFF clusters, since the selection criteria of the HFF systems can introduce bias towards massive and complex cluster systems. In fact, MACS J0416 shows a very elongated and bimodal mass distribution which is not the case for the selected simulated cluster.

BUFFALO will be of a major importance to confirm and characterize the substructures detected in the cluster field, mainly those close to the edges of the FOV, and thus understand better the build-up and merging scenario in place in MACS J0416. Moreover, the overall projected density distribution of the parallel field seems to be connected with the cluster. BUFFALO data will link both fields, and will thus shed light on this possible connection. This work is just a glimpse into the promising data that future surveys will provide in order to strengthen our understanding of these giant galaxy cluster systems.

ACKNOWLEDGEMENTS

We are grateful to the anonymous referee for his/her comments that improved the manuscript. We kindly thanks Liliya Williams and Johannes Schwinn for their comments that improved the work. This work is based on data and catalogue products from HFF-DeepSpace, funded by the National Science Foundation and Space Telescope Science Institute (operated by the Association of Universities for Research in Astronomy, Inc., under NASA contract NAS5-26555). This project has received funding from the European Union's Horizon 2020 Research and Innovation Programme under the Marie Sklodowska-Curie grant agreement No 734374. This work was partially supported by the Consejo Nacional de Investigaciones Científicas y Técnicas (CONICET, Argentina) and the Secretaría de Ciencia y Tecnología de la Universidad Nacional de Córdoba (SeCyT-UNC, Argentina). We made an extensive use of the following python libraries: http://www.numpy.org/, http://www.scipy.org/, and http://www.matplotlib.org/. This research made use of Astropy,[7] a community-developed core PYTHON package for Astronomy (Astropy Collaboration 2013; Price-Whelan et al. 2018). MJ is supported by the United Kingdom Research and Innovation (UKRI) Future Leaders Fellowship 'Using Cosmic Beasts to uncover the Nature of Dark Matter' (grant number MR/S017216/1). This project was also supported by the Science and Technology Facilities Council [grant number ST/L00075X/1]. DH is supported by the D-ITP consortium, a program of the Netherlands Organization for Scientific Research (NWO) that is funded by the Dutch Ministry of Education, Culture and Science (OCW). MS is supported by the Netherlands Organization for Scientific Research (NWO) VENI grant 639.041.749.

REFERENCES

Acebron A. et al., 2019, ApJ, 874, 132
Astropy Collaboration, 2013, A&A, 558, A33
Bahé Y. M. et al., 2017, MNRAS, 470, 4186
Balestra I. et al., 2016, ApJS, 224, 33
Barnes D. J. et al., 2017, MNRAS, 471, 1088
Bartelmann M., Maturi M., 2017, Scholarpedia, 12, 32440
Bertin E., Arnouts S., 1996, A&AS, 117, 393
Brammer G. B., van Dokkum P. G., Coppi P., 2008, ApJ, 686, 1503
Caminha G. B. et al., 2017, A&A, 600, A90
Coe D., Bradley L., Zitrin A., 2015, ApJ, 800, 84
Connor T., Kelson D. D., Donahue M., Moustakas J., 2019, ApJ, 875, 16
Crain R. A. et al., 2015, MNRAS, 450, 1937
Davis M., Efstathiou G., Frenk C. S., White S. D. M., 1985, ApJ, 292, 371
Diego J. M., Tegmark M., Protopapas P., Sand vik H. B., 2007, MNRAS, 375, 958
Dietrich J. P., Werner N., Clowe D., Finoguenov A., Kitching T., Miller L., Simionescu A., 2012, Nature, 487, 202
Dolag K., Borgani S., Murante G., Springel V., 2009, MNRAS, 399, 497
Ebeling H., Edge A. C., Henry J. P., 2001, ApJ, 553, 668
Ebeling H., Ma C.-J., Barrett E., 2014, ApJS, 211, 21
Eckert D., Molendi S., Paltani S., 2011, A&A, 526, A79
Eckert D. et al., 2017, A&A, 605, A25
Elíasdóttir Á. et al., 2007, preprint (arXiv:0710.5636)
Giles P. A. et al., 2016, A&A, 592, A3
Gonzalez E. J. et al., 2018, A&A, 611, A78
Grillo C. et al., 2015, ApJ, 800, 38
Gruen D. et al., 2014, MNRAS, 442, 1507
Harvey D., Massey R., Kitching T., Taylor A., Tittley E., 2015, Science, 347, 1462
Harvey D., Kneib J. P., Jauzac M., 2016, MNRAS, 458, 660
Harvey D., Tam S.-I., Jauzac M., Massey R., Rhodes J., 2019, preprint (arXiv:1911.06333)
Hickox R. C., Markevitch M., 2006, ApJ, 645, 95
Ishigaki M., Kawamata R., Ouchi M., Oguri M., Shimasaku K., Ono Y., 2018, ApJ, 854, 73
Jauzac M. et al., 2012, MNRAS, 426, 3369
Jauzac M. et al., 2014, MNRAS, 443, 1549
Jauzac M. et al., 2015a, MNRAS, 446, 4132
Jauzac M. et al., 2015b, MNRAS, 452, 1437
Jauzac M. et al., 2016, MNRAS, 463, 3876
Jauzac M. et al., 2018, MNRAS, 481, 2901
Johnson T. L., Sharon K., Bayliss M. B., Gladders M. D., Coe D., Ebeling H., 2014, ApJ, 797, 48
Jullo E., Kneib J. P., 2009, MNRAS, 395, 1319
Jullo E., Kneib J. P., Limousin M., Elíasdóttir Á., Marshall P. J., Verdugo T., 2007, New J. Phys., 9, 447
Jullo E., Pires S., Jauzac M., Kneib J. P., 2014, MNRAS, 437, 3969
Kaiser N., Squires G., 1993, ApJ, 404, 441
Kneib J.-P., 2010, European Astronomy, Astrophysics and Space Science Proceedings. Springer Science+Business Media B.V., p. 183
Kneib J.-P., Natarajan P., 2011, A&AR, 19, 47
Koekemoer A. M. et al., 2011, ApJS, 197, 36
Lam D., Broadhurst T., Diego J. M., Lim J., Coe D., Ford H. C., Zheng W., 2014, ApJ, 797, 98
Leauthaud A. et al., 2007, ApJS, 172, 219
Lieu M. et al., 2016, A&A, 592, A4
Lotz J. M. et al., 2017, ApJ, 837, 97
Mahler G. et al., 2019, ApJ, 873, 96
Mann A. W., Ebeling H., 2012, MNRAS, 420, 2120
Meneghetti M. et al., 2017, MNRAS, 472, 3177
Munari E. et al., 2016, ApJ, 827, L5
Natarajan P., Springel V., 2004, ApJ, 617, L13
, P., De Lucia G., Springel V., 2007, MNRAS, 376, 180
Natarajan P. et al., 2017, MNRAS, 468, 1962
Niemiec A., Jauzac M., Jullo E., Limousin M., Sharon K., Kneib J.-P., Natarajan P., Richard J., 2020, MNRAS, 493, 3331
Ogrean G. A. et al., 2015, ApJ, 812, 153
Planck Collaboration XVI, 2014, A&A, 571, A16
Postman M. et al., 2012, ApJS, 199, 25
Price-Whelan A. M. et al., 2018, AJ, 156, 123

[7] http://www.astropy.org.

Reed B., Remolian J., Sharon K., Li N., SPT Clusters Cooperation, 2018, AAS Meeting Abstracts #231. p. 258.06
Remolina González J. D., Sharon K., Mahler G., 2018, ApJ, 863, 60
Rhodes J., Refregier A., Groth E. J., 2000, ApJ, 536, 79
Rhodes J. D. et al., 2007, ApJS, 172, 203
Richard J. et al., 2014, MNRAS, 444, 268
Schaller M., Dalla Vecchia C., Schaye J., Bower R. G., Theuns T., Crain R. A., Furlong M., McCarthy I. G., 2015, MNRAS, 454, 2277
Schaye J. et al., 2015, MNRAS, 446, 521
Schwinn J., Jauzac M., Baugh C. M., Bartelmann M., Eckert D., Harvey D., Natarajan P., Massey R., 2017, MNRAS, 467, 2913
Sebesta K., Williams L. L. R., Mohammed I., Saha P., Liesenborgs J., 2016, MNRAS, 461, 2126
Sereno M., Umetsu K., 2011, MNRAS, 416, 3187
Sharon K., Johnson T. L., 2015, ApJ, 800, L26
Sharon K. et al., 2019, ApJ, 247, 12
Shipley H. V. et al., 2018, ApJS, 235, 14
Springel V., White S. D. M., Tormen G., Kauffmann G., 2001, MNRAS, 328, 726
Steinhardt C. L., Capak P., Masters D., Speagle J. S., 2016, ApJ, 824, 21
Steinhardt C., Jauzac M., Capak P., Koekemoer A., Oesch P., Richard J., Sharon K. q., BUFFALO, 2018, AAS Meeting Abstracts #231. p. 332.04
Treu T. et al., 2015, ApJ, 812, 114
Umetsu K. et al., 2014, ApJ, 795, 163
Vegetti S., Koopmans L. V. E., Bolton A., Treu T., Gavazzi R., 2010, MNRAS, 408, 1969
Wambsganss J., 2006, Ann. Phys., 15, 43
Wegner G. A., Heymans C. E., 2011, AAS Meeting Abstracts #218. p. 319.04
Williams L. L. R., Sebesta K., Liesenborgs J., 2018, MNRAS, 480, 3140
Zitrin A., Broadhurst T., Rephaeli Y., Sadeh S., 2009, ApJ, 707, L102

This paper has been typeset from a TEX/LATEX file prepared by the author.